Energy 286 (2024) 129427

Contents lists available at ScienceDirect

Energy

journal homepage: www.elsevier.com/locate/energy

Experimental investigation of a dual-pontoon WEC-type breakwater with a hydraulic-pneumatic complementary power take-off system

Yong Cheng [a], Fukai Song [a], Lei Fu [a], Saishuai Dai [b,*,1], Zhiming Yuan [a,b], Atilla Incecik [b]

[a] School of Naval Architecture and Ocean Engineering, Jiangsu University of Science and Technology, Zhenjiang, 212003, China
[b] Naval Architecture, Ocean and Marine Engineering Department, University of Strathclyde, Glasgow, United Kingdom

ARTICLE INFO

Handling Editor: Prof G Iglesias

Keywords:
Floating breakwater
Wave energy converter
Dual-pontoon structure
Oscillating buoy
Oscillating water column

ABSTRACT

Floating offshore multi-purpose structures have recently attracted much attention worldwide in terms of sharing costs, enhancing efficiencies and reducing environmental impacts. In this paper, hydrodynamic experiments are conducted to examine the accessibility of wave energy absorption by a dual-pontoon floating breakwater integrated with hybrid-type wave energy converters (WECs). The main structure and the air chamber between the two pontoons are designed as an Oscillating Buoy (OB) and an Oscillating Water Column (OWC), respectively. Two power take-off (PTO) systems, including a hydraulic system and a Wells turbine, are selected to extract wave energy from structural motion and chamber airflow. To investigate the hydraulic-pneumatic complementary effects, PTO damping coefficients of two systems are adjusted both individually and synchronously. Besides, the hydrodynamic comparison among different geometrical parameters, are further studied. The breakwater-integrated hybrid WEC system led to a larger optimal pneumatic damping for the OWC while the optimal hydraulic damping for the OB is not affected. Additionally, the internal air pressure is acting as a resistive force to pontoons, hence the pontoon motion is smaller, and part of the kinematic energy from pontoons is extracted by the OWC. Correspondingly, the wave attenuation capacity is enhanced by multiple harvesting manners, especially for long-period waves.

1. Introduction

Mitigating global warming and environmental pollution derived from the utilisation of fossil energy, has been targeted by European Commission which declares at least 40% cuts in greenhouse gas emissions (from 1990 levels) and 32% share for renewable energy in the 2030 Climate and Energy Framework [1]. Marine Renewable Energy (MRE) provides an alternative solution to promote energy transition from fossil energy to clean energy and achieve a sustainable development plan. Wave energy as one of MRE resources, has motivated wide attention due to its high energy density, lasting consistency and minimal negative ecological impact [2]. The available power per unit of wave crest is estimated at 37 kW/m and 33 kW/m for the U.S. North Pacific and North Atlantic coasts, respectively [3]. Thus, significant strides have been taken towards the development of wave energy conversion (WEC) technologies [4]. Ocean Energy Europe (OEE) claimed that the cumulative global wave energy installations have consistently grown to 12.7 MW since 2010 and will increase by 3.8 MW in 2022 [5].

Oscillating Water Column (OWC) and Oscillating Buoy (OB) WECs as two dominant devices at this stage because of their geometric and mechanical simplicity. An OWC s device often consists of a partially submerged hollow-hull structure with openings at both ends. Usually, air is trapped between the water surface and a Power Take-Off (PTO) system. The trapped air is exhaled and inhaled through the PTO system (e.g. air turbine coupled to a generator) when subject to waves, power is then generated [6]. Many experiments and numerical studies about OWC have been carried out in the past decade. For example, He and Huang [7] developed an OWC device with two different shapes of orifices to simulate the nonlinear PTO mechanism and reconstructed the instantaneous spatial profile of the free-surface in the chamber based on a two-point measurement method. Konispoliatis and Mavrakos [8] analysed the array of floating OWCs based on the linearised potential flow theory and calculated the wave loads. The simulated results suggest that the number and distance of OWCs at the location of the wave front significantly affect the power capture efficiency. In 2015, Ning et al. [9] numerically studied the hydrodynamics of a coastal OWC based on the

* Corresponding author
E-mail address: saishuai.dai@strath.ac.uk (S. Dai).
[1] Mainly research in hydrodynamic performance of wave energy converters.

https://doi.org/10.1016/j.energy.2023.129427
Received 11 June 2023; Received in revised form 7 August 2023; Accepted 19 October 2023
Available online 30 October 2023

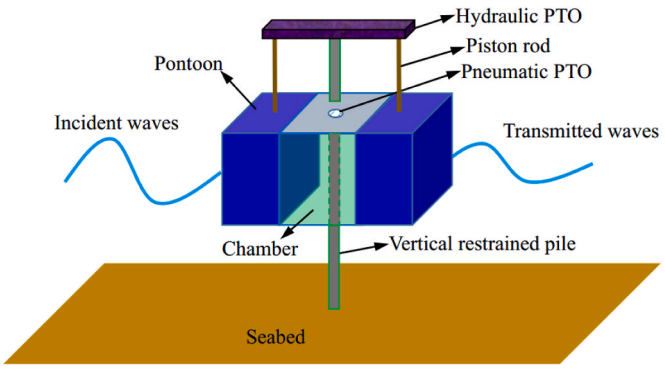

Fig. 1. Schematic sketch of the WEC-floating breakwater integrated system.

Higher-Order Boundary Element Method (HOBEM). The model results revealed the dynamic patterns of the air pressure and free-surface elevation inside the chamber. One year later, to further validate this theoretical finding, Ning et al. [10] followed up with an experimental investigation and found the opening ratio of the OWC plays a decisive role in the maximum conversion efficiency. Ning et al. [11] later presented a cylindrical dual-chamber OWC with an inner chamber and an outer chamber. It was found that the coupled effect between two chambers shifts resonant frequencies and expands the effective frequency bandwidth. Molina et al. [12] investigated the air turbine characteristics of a separate OWC on which the aerodynamic power depends. Portillo et al. [13] implemented a numerical linear turbine of the bent-duct OWC based on linear wave theory in the frequency domain and conducted a parametric sensitivity analysis in both backward and frontward configurations. The results illustrated that the frontward configurations presented a better performance under the tested conditions.

OB device typically comprises a pontoon or floater with a certain degree of freedom, fitted with a translational PTO to generate power in the direction of motion. Windt et al. [14] utilised the Computational Fluid Dynamics (CFD) method to study the scaled-down Wavestar WEC [15] and found that the hydrodynamic scaling effect on the total load of WEC with a hemispherical bottom can be ignored. Based on the Boundary Discretisation Method (BDM), point-absorbing WECs with different shapes of the vertical axis symmetry, including parabolic, cylindrical and conical, were numerically investigated by Zhang et al. [16]. Renzi et al. [17] applied the mathematical theory to explain the motion of the Oyster as a flap-type absorber accurately. Goggins and Finnegan [18] established the optimal structural geometry configuration for the Atlantic marine energy test spot and derived the optimal configuration for devices with different radius. Wang et al. [19] combined an OB in the heave mode and a perforated wall using the linear potential flow theory. This design not only widened the capture width ratio of the OB, but also enhanced the energy extraction of the combined system. Robertson et al. [20] summarised the operating principles of different OB architectures, including single-body OB, two-body OB and multi-body OB, and developed an empirically calculable and easily implemented wave-to-electricity model to quantify energy production performance.

The relatively high Levelized Cost of Energy (LCoE) and Net Present Value (NPV) of wave energy compared to other energy sources (i.e. offshore wind energy) continue to hinder further large-scale commercial promotion [21]. To reduce this high LCOE, several solutions have been proposed, among which the integration of multi-type WEC technologies is a viable option to optimise its hydrodynamic performance and configuration design. Fonseca et al. [22] measured the air pressure, mooring forces and buoy's motion of the OWC spar-buoy. The tested result revealed that shutting down the chamber reduces the damping effect induced by the air turbine but amplifies the motion of the model. Cui et al. [23] proposed a hybrid cylindrical OWC-OB at a three-dimensional analytical model, where an OB is hinged to the wall of an OWC, and modelled the conversion efficiency of the device layouts and incident wave directions. It is concluded that the OWC-OB hybrid system outperforms the isolated WECs in terms of the effective frequency bandwidth. Wang and Zhang [24] developed a theoretical model via the eigenfunction matching schemes. The mixed WECs comprise a torus OB and a concentric cylindrical system was studied. Cheng et al. [25] deployed a small-size OB at the centre of the free surface within the OWC chamber and investigated the hydrodynamics of the concept based on HOBEM. The resonant motion of the OB device inside the chamber enhances the maximum capture efficiency and the frequency bandwidth. Following this investigation, Cheng et al. [26] deployed an OB upstream from an OWC, and tested their respective wave energy extraction experimentally. Nguyen et al. [27] introduced dual-mode WECs attached to a large floater, which showed the complementary function for wave energy extraction from a floating auxiliary plate and a submerged vertical plate across the wave periods range investigated.

By optimising the geometric design i.e. attaching WECs to floaters, WECs with an acceptable wave-attenuation performance can be considered as effective breakwaters. These multi-target and multi-function concepts further broaden WEC's commercial market. Mustapa et al. [28] reviewed the integration of different type WECs and fixed breakwater. Zhao et al. [29] further emphasised the research priority of floating breakwater integrating with WECs. He et al. [30] proposed an analytical model to investigate a pile-supported breakwater-type OWC. Theoretical results showed that, with optimal PTO damping, the device demonstrated excellent energy conversion efficiency and transmission performance. Based on the identical analytical method, Guo et al. [31] designed a novel OWC breakwater, which is equipped with a front-wall oscillating in pitch mode. It is shown that the pitching front wall extensively broadened the frequency bandwidth and the narrower front-wall width contributed to the energy conversion performance. Howe et al. [32] tested a floating breakwater integrated with the multiple OWCs, and indicated that device-to-device interaction exerts a constructive or destructive effect on energy extraction depending on incident wave frequencies. Zhang et al. [33] created a CFD-based numerical flume and examined the OB breakwater with different bottom shapes. The triangular-baffle bottom buoy was considered as the most efficient and effective configuration in terms of coastal protection and energy conversion. Zhao et al. [34] treated a multi-chamber WEC as a floating breakwater and compared the performance of OWC-breakwaters with different numbers of air chambers. The physical study showed that the hydrodynamic interactions between multi-chambers enhance wave energy extraction and wave attenuation in long waves. Cheng et al. [35] compared the hydrodynamic coefficient of the single-pontoon OB and dual-pontoon OWC numerically and experimentally. It is demonstrated that the performance of the OWC-breakwater integrated system with the asymmetrical pontoon drafts is better than that of the OB-breakwater.

Existing hydrodynamic studies primarily focus on the WEC-breakwater integrated systems with a single-mode PTO system or multiple WECs isolated from each other. The wave radiation and resonance in the gap between the WECs tend to have a significant interference effect. The hydrodynamic performance of a WEC-type breakwater with a multi-mode PTO system is less explored. The motivation of this paper is to propose a dual-pontoon WEC-type breakwater with a hydraulic-pneumatic complementary PTO system, which incorporates energy extraction principles of both OBs and OWCs. The experimental comparisons among a WEC-breakwater with a hydraulic, a pneumatic and a hybrid PTO system are discussed comprehensively. Furthermore, the performance dependence on the designed parameters is also examined, aiming to optimise the configuration of WEC-breakwater integration. The outcome of the current study has the potential to further improve power extraction and reduce LCoE for such kind multi-purpose renewable energy platforms.

The paper is organised as follows: Section 2 describes the

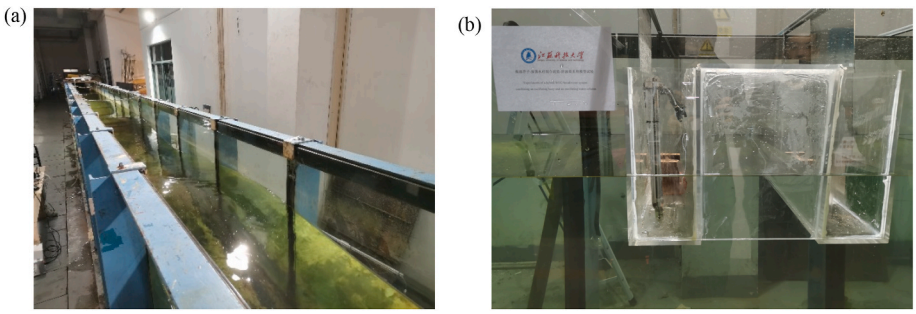

Fig. 2. Photos of (a) wave flume and (b) dual-pontoon WEC-floating breakwater integrated system.

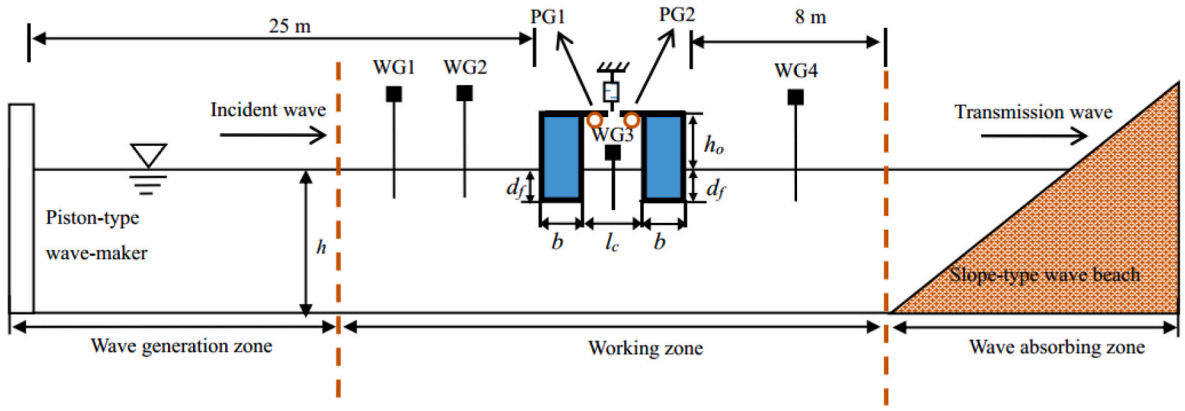

Fig. 3. Experimental setup of dual-pontoon hybrid-type WEC system.

Table 1
Model parameters of the WEC-type floating breakwater.

Pontoon draft d_f (m)	Pontoon width b (m)	Chamber width l_c (m)	Opening diameter d_o (m)	PTO damping b_{pto} (Ns/m)
0.15	0.15	0.25	0.025, 0.035, 0.045, 0.055	90, 150, 200, 300
0.10	0.15	0.25	0.025	150
0.20	0.15	0.25	0.025	150
0.15	0.15	0.15	0.025	150
0.15	0.15	0.35	0.025	150

experimental setup and the tested data analysis i.e. the heave body motion, the wave surface variation, the hydrodynamic coefficients, and the energy conversion efficiency. Section 3 establishes a computational fluid dynamic (CFD) model to investigate the proposed concept numerically. In Section 4, the results will be presented and followed by a discussion.

2. Experiment description

2.1. Model design

A novel dual-pontoon floating breakwater combining an OB and an OWC is proposed in the current study, as shown in Fig. 1. An air chamber is formed between the two pontoons, and can be regarded as an OWC device without alternating the geometry of the floating breakwater. An air turbine is installed on the top nozzle of the chamber and is driven by the internal oscillating airflow. The floating breakwater is restrained by a vertical pile, and thus only heaving motion is released to drive a hydraulic PTO system through the OB working mechanism. Thereby, the incident wave energy can be extracted in the form of air pressure energy and the floater kinetic energy by the above-mentioned two PTO systems. On the other hand, the coupled interaction between the two WEC devices could change the wave energy absorption, which may affect the wave attenuation capacity and the wave energy conversion efficiency. The interaction between the two WECs depends on design parameters like spacing between the two pontoons. The current study aims to find an optimal design configuration that provides the best energy extraction and wave attenuation performance.

2.2. Experimental layout

Scaled experiments of the WEC-type floating breakwater system were performed in the 40 m (length) × 0.8 m (width) × 1.4 m (depth) wave flume at the Jiangsu University of Science and Technology, China, as shown in Fig. 2. A piston-type wavemaker is installed at one end of the flume. At the other end of the tank, a slope-type wave beach is employed to absorb the incoming waves. During the test, resistance-type wave probes were deployed inside the flume at multiple locations during the test to measure wave elevations and OWC response. An optical motion-tracking system was adopted to measure the heave response of the pontoon. Finally, the pressure inside the air chamber and force acting on the hydraulic PTO were recorded via a differential pressure transducer and a load cell, where the pressure transducer is calibrated in the range of ±500 Pa, while the load cell is calibrated to 15 kg. Signals are sampled at 100 Hz.

A scale factor of 1:20 based on the Froude scaling law was chosen for the experiment, considering the physical size of the flume. The dual-pontoon structure was made by 0.01-m thick Perspex sheets. The model was deployed in the working zone of the flume as shown in Fig. 3 i.e. 25 m away from the wavemaker, to maximise the effective test time window (Within which the measurements are less likely to be contaminated by reflection from the beach and the wavemaker.). The wave period range conducted in experiments was from $T_w = 0.7$ s–2.1 s, with a fixed incident wave height of $H_i = 0.1$ m. The water depth was set to $h =$

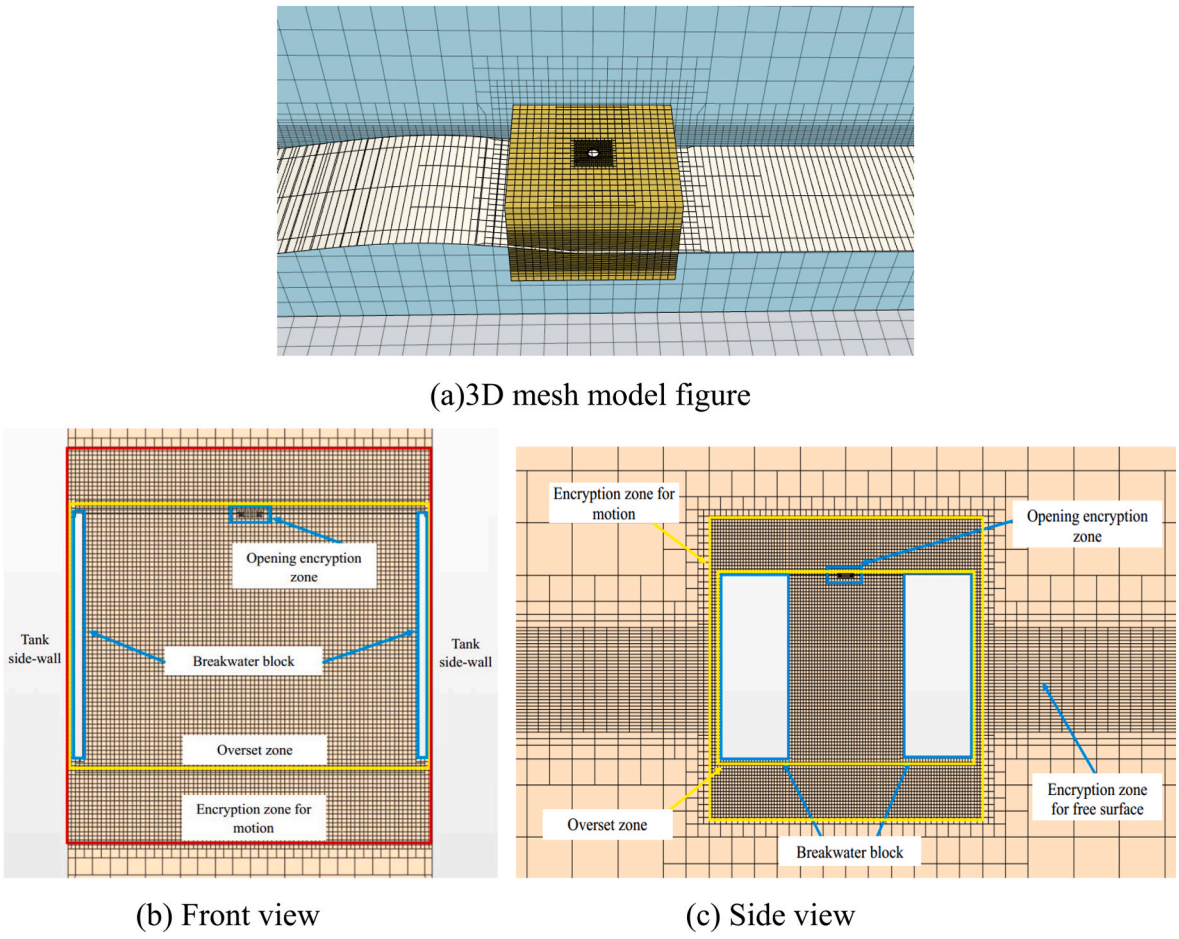

Fig. 4. Mesh generation in CFD simulation.

1.0 m.

In order to reduce the energy loss induced by the lateral gaps between the breakwater and the flume side walls, the breakwater length, perpendicular to the wave propagating direction, was set to 0.78 m. Two pontoons have identical dimensions and three drafts, i.e. d_f = 0.10 m, 0.15 m, and 0.20 m were considered. The width of the two pontoons, b = 0.15 m, was kept the same for all the tests. Three sets of different chambers width between the two pontoons were considered, i.e. l_c = 0.15 m, 0.25 m and 0.35 m. The breakwater is supported by two slide rails installed above the two pontoons, and an aerodynamic damper representing the PTO system of the OB WEC was attached to the pontoon top to absorb the heave kinetic energy of the breakwater (see Fig. 3 for details.). The aerodynamic damping coefficient can be changed by adjusting the damping nozzle, and the corresponding working principle has been described in Ref. [35]. The PTO system for the OWC WEC was represented by an orifice on the roof of the chamber between pontoons and extracted wave energy from the water column oscillation in the chamber. The PTO damping coefficient of the OWC device was determined by the orifice size. In order to explore the complementary effect between the two PTO systems, different combinations of aerodynamic damping coefficients, i.e. b_{pto} = 90 N/m, 150 N/m, 200 N/m, 300 N/m and orifice opening diameters, i.e. d_o = 0.025 m, 0.035 m, 0.045 m, 0.055 m are selected. The details of the experimental model are summarised in Table 1.

2.3. Data analysis

Four wave gauges (i.e. WG1 to WG4) indicated in Fig. 3 were placed along the wave propagating direction to measure water-wave elevation. The wave attenuation performance of the integrated system as a floating breakwater is weighed by the wave reflection and transmission coefficients defined as following

$$K_r = \frac{H_r}{H_i} \tag{1}$$

$$K_t = \frac{H_t}{H_i} \tag{2}$$

where K_r and K_t denote the reflection and transmission coefficients, respectively. H_r is the reflected wave height obtained by separating data of WG1 and WG2 using a two-point approach [36], and H_t is the transmitted wave height measured directly by WG4. The OWC response in the chamber is denoted by wave coefficient K_o

$$K_o = \frac{H_o}{H_i} \tag{3}$$

where H_o is the height of the oscillation of the free surface inside the chamber and was recorded by WG3.

The period-averaged extracted power by the OB [33] and the OWC [7] can be calculated via

$$E_{p1} = \frac{1}{nT}\int_t^{t+nT} b_{pto}\cdot\left|\frac{d\zeta}{dt}\right|^2 dt \tag{4}$$

$$E_{p2} = \frac{1}{nT}\int_t^{t+nT} A_w\cdot\sqrt{\frac{2|\overline{P}|^3}{\rho_a C_d}}dt \tag{5}$$

where subscripts 1 and 2 denote the OB and the OWC devices, respec-

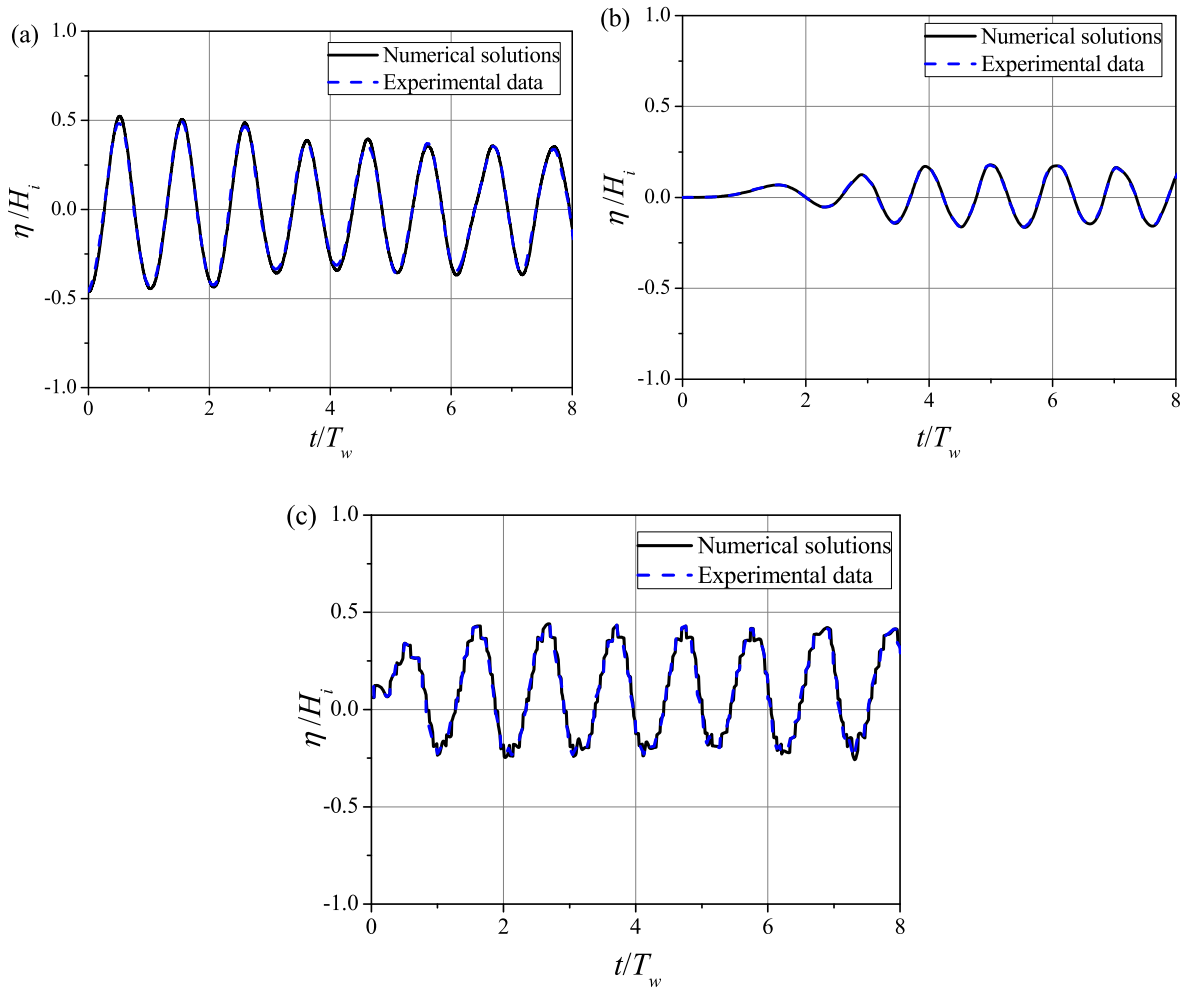

Fig. 5. Time series of the measured and simulated wave elevations at (a) WG 1, (b) WG 4 and (c) WG 3.

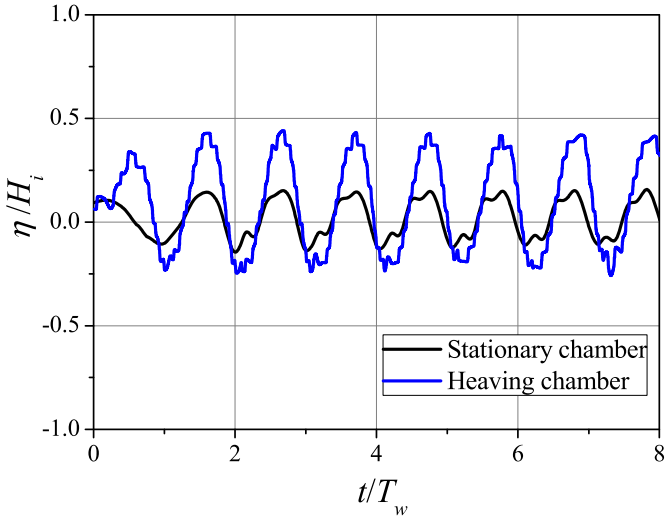

Fig. 6. Comparisons of the wave elevation in heaving and stationary chambers.

tively. ζ is the heaving displacement of the floating breakwater, A_w is the water-plane area of the chamber, ρ_a is the air density. $\overline{P} = (P_1 + P_2)$ is the average air pressure in the chamber, in which P_1 and P_2 are measured by pressure gauges PG1 and PG2. C_d is the pneumatic damping coefficient of the OWC device, which is calculated based on the opening ratio α of the orifice [37]

$$C_d = \left[\frac{1}{\alpha\left(\frac{1}{0.639\sqrt{1-\alpha}+1}\right)} - 1\right]^2 \tag{6}$$

Thus, the overall wave conversion efficiency R of WEC devices is expressed

$$R = R_1 + R_2 \tag{7}$$

where $R_1 = E_{p1}/E_w$ and $R_2 = E_{p2}/E_w$ denote the energy conversion efficiency of OB and OWC devices, respectively. Here, the input energy E_w of incident waves is calculated through linear wave theory

$$E_w = \frac{1}{4}\rho_w g A_i^2 \frac{\omega}{k}\left(1 + \frac{2kh}{\sinh 2\,kh}\right) \tag{8}$$

where ρ_w is the water density, g is the gravity acceleration, k is the wave number and ω is the circular frequency. For waves without considering the current effect, the wave number and the wave frequency satisfy the following dispersion relationship

$$\omega = \sqrt{gk\tanh kh} \tag{9}$$

3. Numerical validation

To assist the understanding of the hydrodynamics, a viscous-flow numerical model is established by using the software STAR-CCM+ based on the Finite Volume Method (FVM). In the model, the

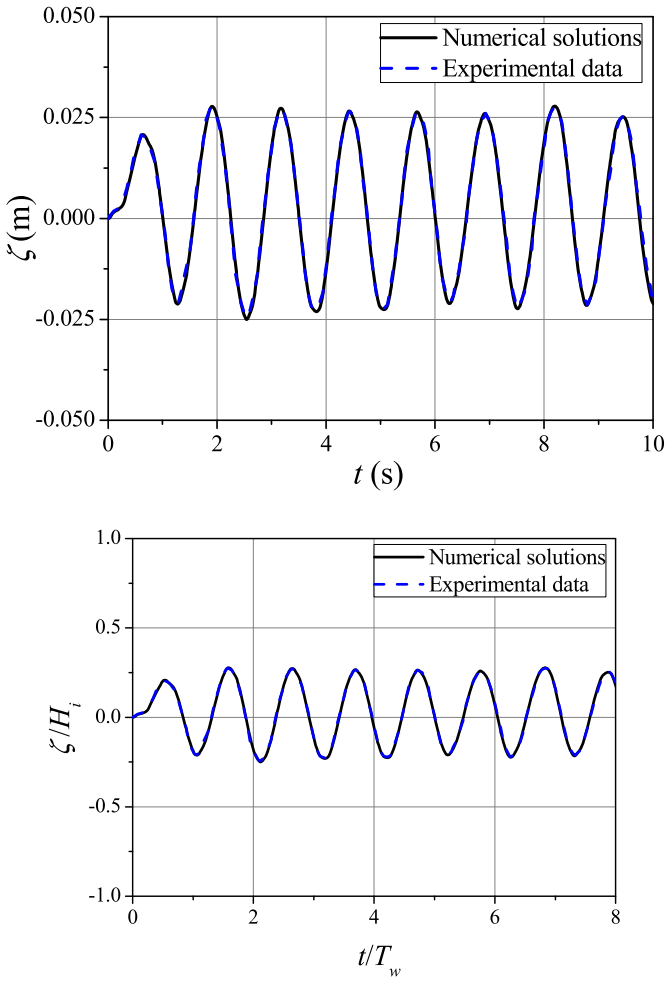

Fig. 7. Time series of the measured and simulated motion response of dual-pontoon heaving breakwater.

computational domain was divided into three parts, i.e. wave-making zone, interacting zone and wave-dissipating zone. The WEC-type floating breakwater is established in the interacting zone, and its heaving motion is realised by using a dynamic meshing scheme. Two PTO systems corresponding to the OB and OWC devices are taken into account by using a linear mechanical damping coefficient and a pneumatic model, respectively. Different from most of the previously mentioned numerical simulations for single WEC devices, the present model can be applied to investigate the complementary effects of the hydraulic-pneumatic hybrid PTO system for multi-type WECs.

3.1. Numerical model

A three-dimensional wave flume was developed numerically to consider the viscous flow field which can be described by the mass and the momentum conservation equations

$$\frac{\partial u_i}{\partial x_i} = 0 \tag{10}$$

$$\rho_w \frac{\partial u_i}{\partial t} + \rho_w u_j \frac{\partial u_i}{\partial x_j} = -\frac{\partial p}{\partial x_i} + F_i + (\mu + \mu_t)\frac{\partial}{\partial x_j}\left(\frac{\partial u_i}{\partial x_j}\right) + \frac{\partial \tau_{ij}}{\partial x_j} \tag{11}$$

where μ and μ_t denote the flow viscosity and the eddy viscosity, respectively. The subscript $i, j = 1$, 2 and 3 denotes the space coordinate (x, y, z). u_i is the velocity component of the fluid, p is the fluid pressure, F_i is the excited force during numerical simulations. ρ_w is the water density. τ_{ij} is the Reynold stress tensor, and is solved using the shear stress transport (SST) k-ω turbulence equations.

The water-wave surface motion is captured by the Volume of Fluid (VOF) method in which a multi-phase flow model including the water, air is applied to update the interface between phases. The volume ratios of the water, air denoted by v_1, v_2, are calculated by

$$\frac{\partial v_i}{\partial t} + (u_1, u_2, u_3)\cdot\nabla v_i = 0 \tag{12}$$

$$v_1 + v_2 = 1 \tag{13}$$

The length, width and height of the total numerical wave flume was defined as 8λ (λ is the wavelength), 0.8 m and 2 m. The wave generation is realised by imposing velocity inlet at one end, whereas the wave absorption at the other end is achieved by applying the forcing method, which is also applied in the wave-making zone to absorb the reflected and radiated waves from the floating breakwater. The velocity inlet condition is defined as fifth-order Stokes waves [38]. The flume top is set as the pressure outlet boundary condition, and other impermeable boundary conditions, i.e. flume bottom, lateral walls and body surfaces, are assigned as no-slip wall conditions. The entire computational domain is discretised by a series of control volumes, and the coupled problem between the hydrodynamic and aerodynamic behaviours of the hybrid-type WECs are solved using a second-order implicit pressure-based solver [39]. The physical variables are interpolated by means of a quadratic-upwind kinematics algorithm. The governing equations are solved using a second order pressure-based solver with

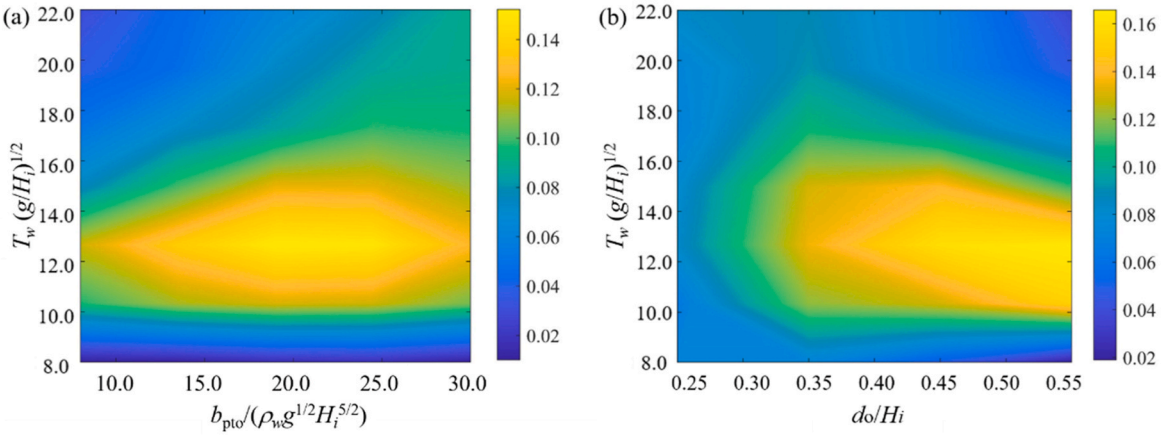

Fig. 8. Efficiency contour of the isolated dual-pontoon (a) OB and (b) OWC as function of PTO dampings. The colour code represents the efficiency with yellow denoting high efficiency and dark blue denoting low efficiency.

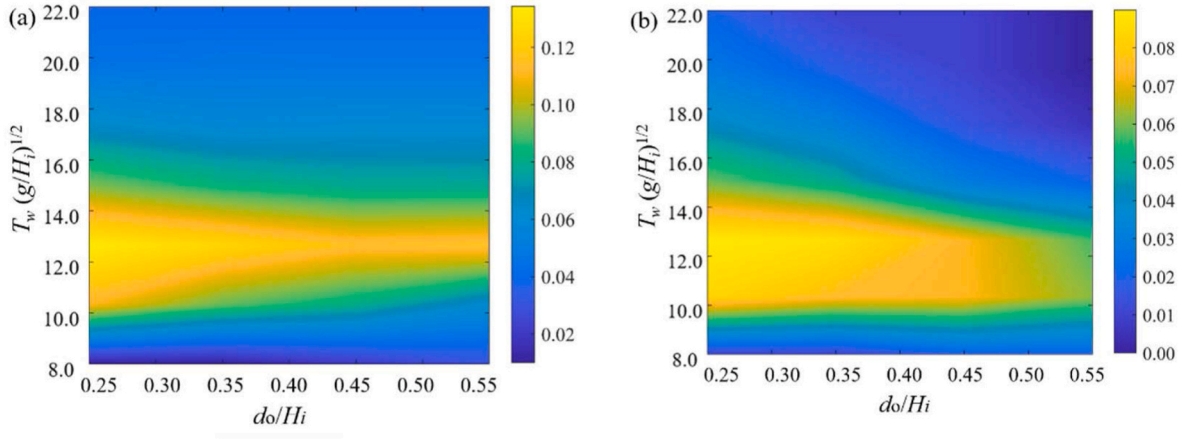

Fig. 9. Efficiency contour of (a) the OB and (b) the OWC within the hybrid-type WEC system as a function of pneumatic dampings.

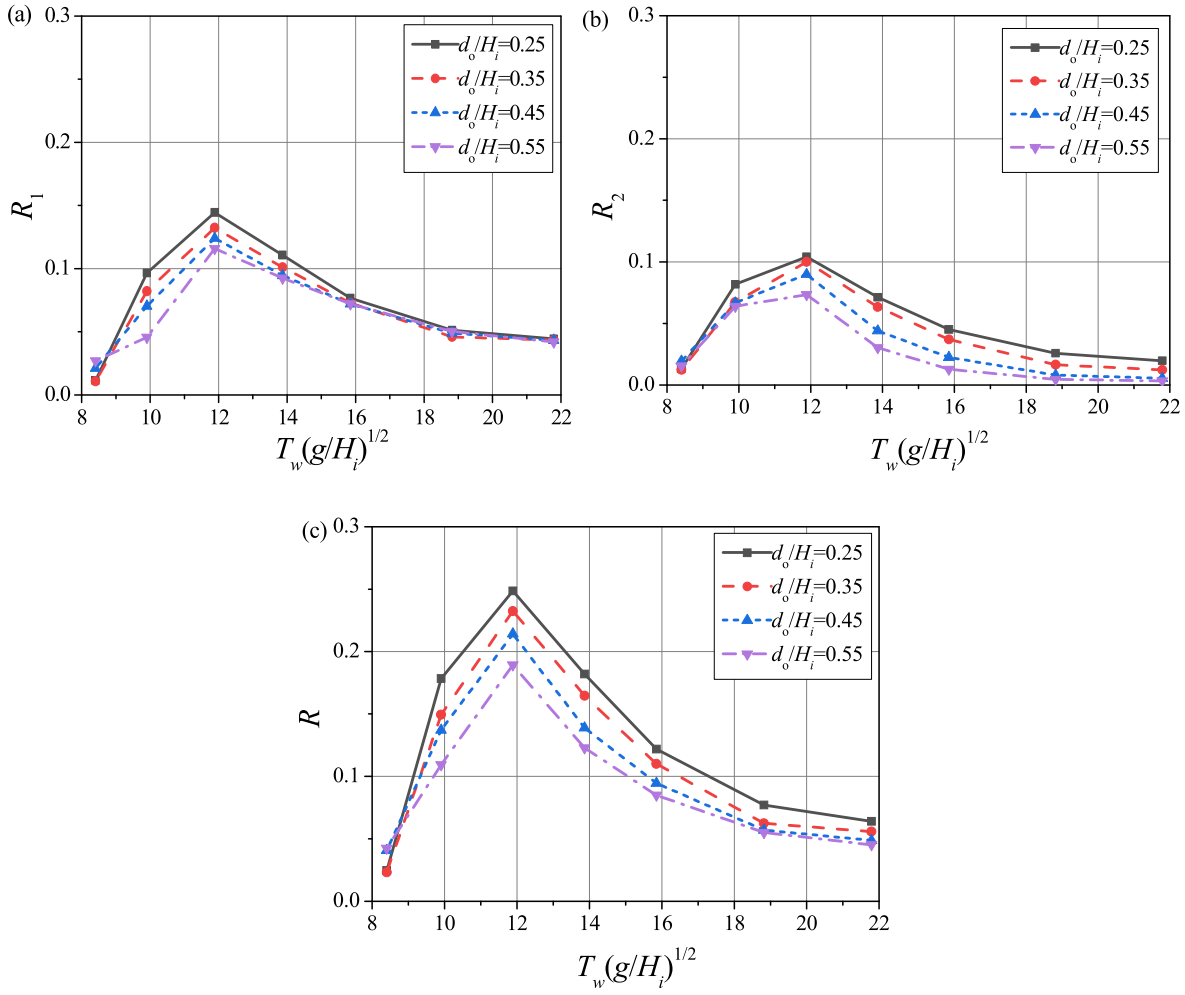

Fig. 10. Variations of the efficiency of (a) the OB, (b) the OWC and (c) the overall system with wave periods and opening diameters.

implicit and unsteady formulations, where the time step is set as $T_w/1000$ according to the converged tests. All numerical solutions satisfy the converged conditions, and all the residuals read less than 0.001.

3.2. Dynamic mesh scheme

In order to ensure numerical accuracy, the meshes discretising the numerical flume were selected with hexahedral cells which were equally distributed by 20 and 80 cells per wave height and per wavelength at least. Mesh was further refined inside the air chamber in order to capture the spatial variation of the OWC. A trimmed mesher is adopted to generate meshes near the water-wave surface, body surface and the transitional zone from fluid to body, as shown in Fig. 4. The floating breakwater was subtracted from the whole computational domain, and then was defined as the heave motion. The pontoon structures were

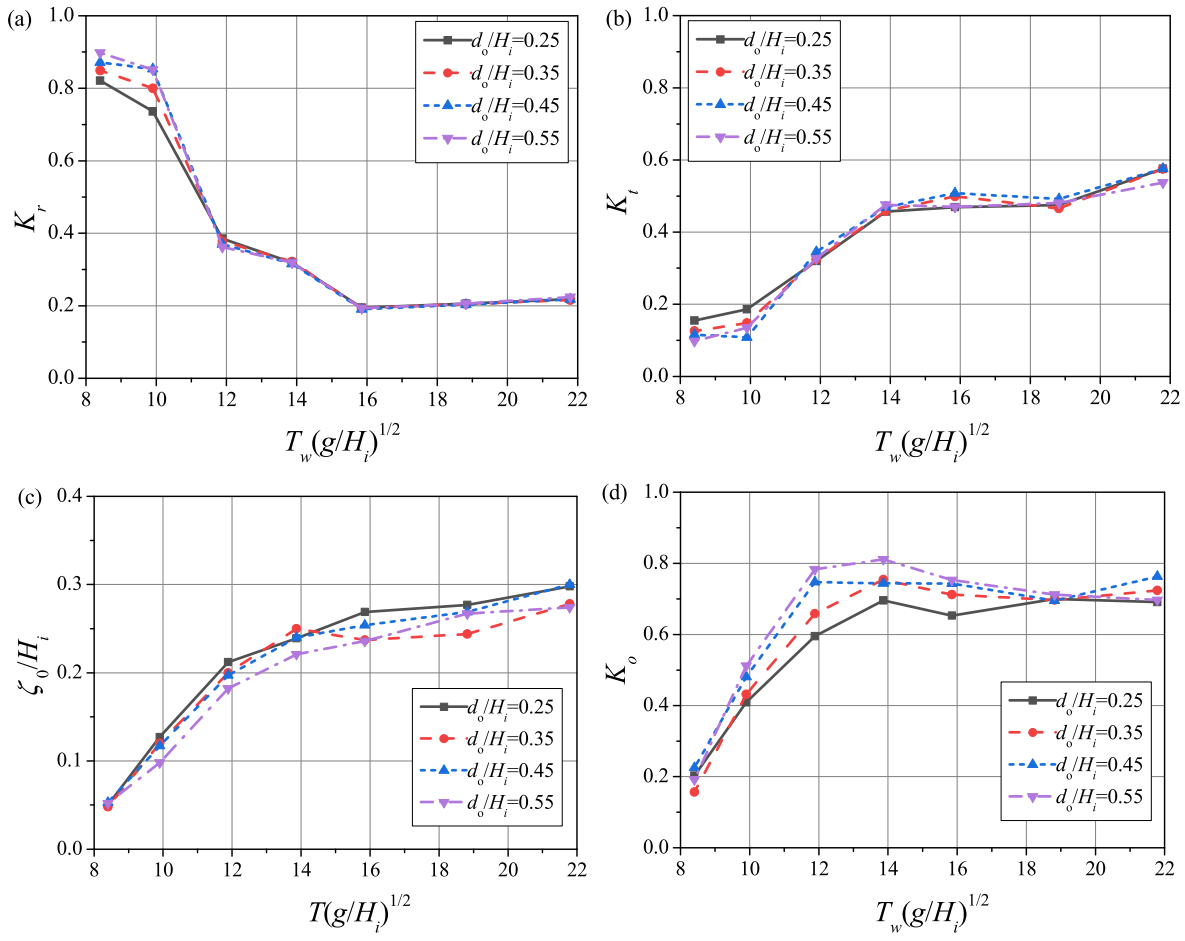

Fig. 11. Variations of (a) the reflection coefficient, (b) the transmission coefficient, (c) the heaving amplitude and (d) the wave coefficient with wave periods and opening diameters.

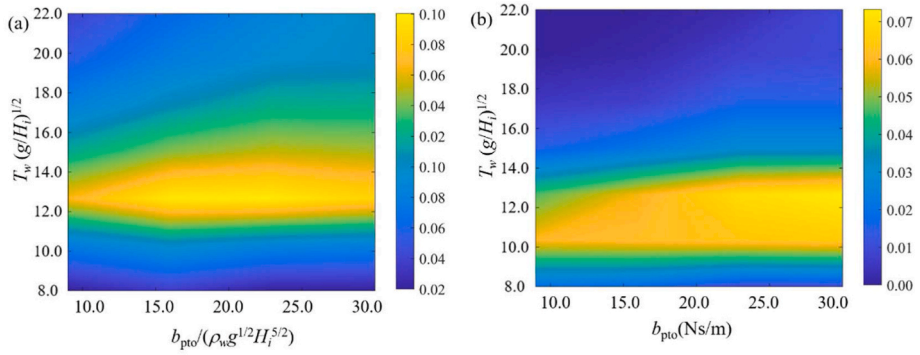

Fig. 12. Efficiency contour of (a) the OB and (b) the OWC within the hybrid-type WEC system as a function of hydraulic dampings.

enclosed by some prismatic layers using a trimmed mesher solver to avoid the mesh distortion caused by the heave motion. An overset dynamic mesher is adopted to update the water and structure motions, in which the complex water-air domain is divided into some simple sub-regions. The flow is independently simulated in each zone and can be overlapped between adjacent sub-regions. The coupled interaction is interpolated according to the category of meshes including active, inactive and acceptor meshes. Thus, the meshes in the domain always maintain good quality as time progresses.

3.3. Validation with experimental data

The numerical model of the proposed device was simulated to compare with experimental results. The model parameters, including geometrical sizes, PTO coefficients and wave conditions, were kept the same as those in the physical experiment. More specifically, the input parameters are given as $d_f/H_i = 1.5$, $b/H_i = 1.5$, $l_c/H_i = 2.5$, $d_o/H_i = 0.25$ m, $b_{pto}/(\rho_w g^{1/2} H_i^{5/2}) = 15$, $T_w(g/H_i)^{1/2} = 11.88$, $h/H_i = 10$, where $H_i =$ 0.1 m. Fig. 5(a)–(c) displays the time series of the water-wave elevation

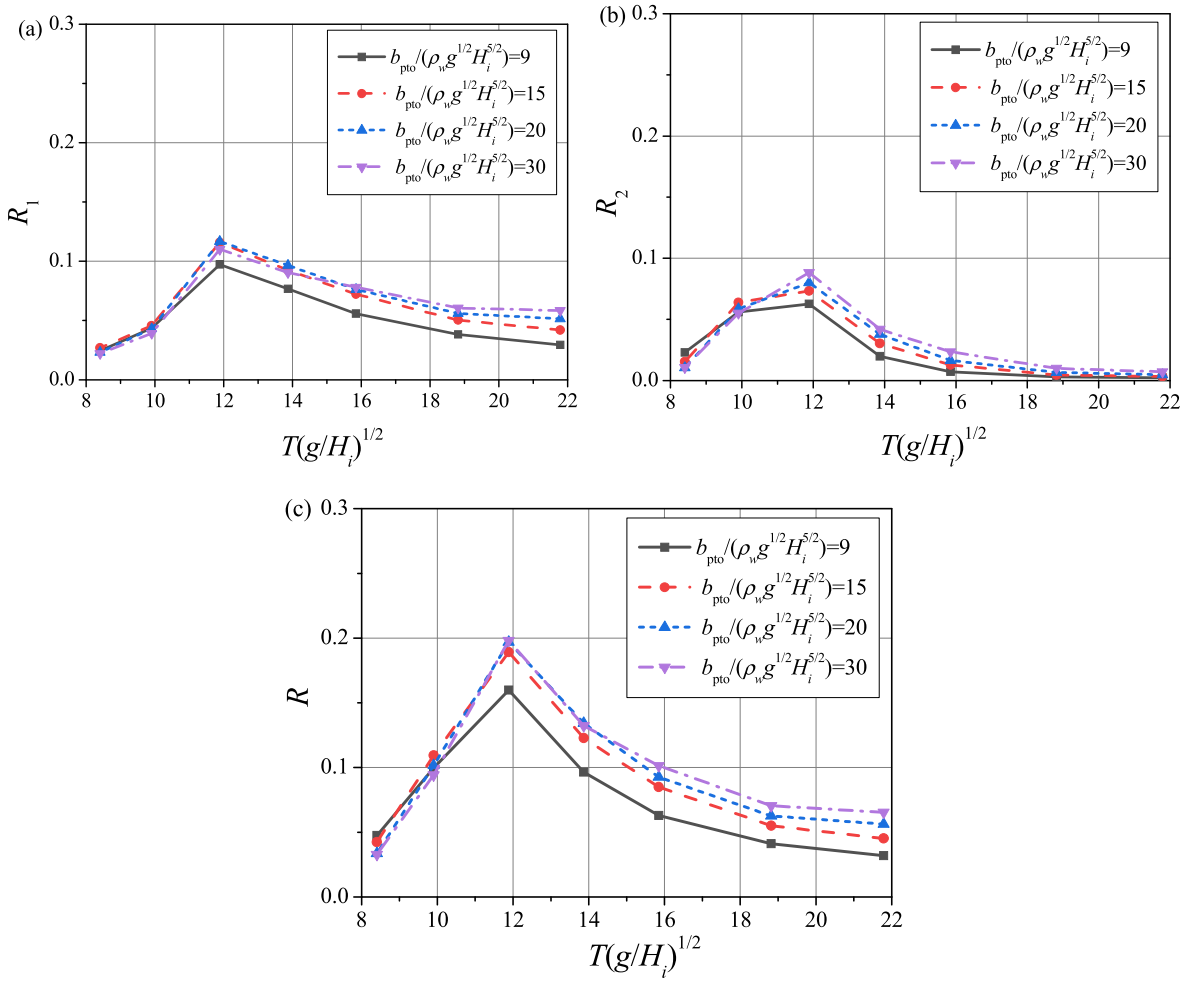

Fig. 13. Variations of the efficiency of (a) the OB, (b) the OWC and (c) the overall system with wave periods and hydraulic dampings.

at WG1, WG4 and WG3. It can be observed from these figures that the numerical solutions correlate well with the measured elevations. Some interesting phenomena are clearly captured by both the CFD model and experiment tests. For example, the water-wave elevation upstream from the breakwater has a reduction when time exceeds 4s, as shown in Fig. 5 (a). This is because the reflected waves by the breakwater interact with the incident waves, leading to partial standing wave groups. It is seen from Fig. 5(b) that the transmitted wave height is significantly smaller than the incident wave height with a transmission coefficient $K_t = 0.37$, indicating the favourable wave-attenuating capacity of the breakwater. It is remarkable from Fig. 5(c) that there are obvious nonlinearities, i.e. climbing-ladder shape on the water-wave elevation curves in the chamber, especially for wave crests and troughs. In order to explain this phenomenon, the water-wave elevation in the chamber of the heaving breakwater is compared with that of a stationary breakwater with the same dimensions, as shown in Fig. 6. It can be illustrated that the heave motion of the breakwater enhances the water column motion in the chamber significantly by three times. On the other hand, the phase difference between the heave motion of the pontoon and the internal water column would also affect the air pressure in the chamber.In addition, the average value of the water-wave elevation is higher than the calm-water surface, which means that the heave motion of the breakwater reduces the air pressure in the chamber when heaving upwards and increases the pressure when heaving downwards.

Fig. 7 shows the time series of the heave motion of the breakwater regarded as an OB device. It is clear that the numerical solutions agree well with the experimental data, further demonstrating that the designed experiments can provide accurate assessment,

4. Experimental analysis

After comparing with numerical solutions, a series of experiments are conducted to investigate the complementary effects of the hydraulic and pneumatic PTO systems, the quantitative difference between stationary and heaving OWCs and the sensitivity of geometrical parameters. The hydrodynamic performance of the WEC-type floating breakwater is mainly assessed based on the reflection coefficient, the transmission coefficient, the wave power conversion efficiency and the effective frequency bandwidth.

4.1. Hydrodynamic performance of isolated PTO systems

In order to discern the complementary effect between the hydraulic and pneumatic PTO systems for the OB-OWC hybrid WEC system, the wave energy conversion efficiency of a dual-pontoon floating breakwater, respectively, treated as an isolated heaving OB and a fixed OWC is tested. The breakwater draft is set as $d_f/H_i = 1.5$. The pontoon width and the chamber width between the two pontoons are $b/H_i = 1.5$ m and $l_c/H_i = 2.5$, respectively. The efficiency contour of the two isolated WEC devices as the function of the PTO damping coefficient is shown in Fig. 8 (a) and (b). Through Fig. 8(a), It can be easily found that the maximum efficiency of the isolated OB device occurs at $T_w(g/H_i)^{1/2} = 11.88$ which is the resonant period of the OB, and corresponds the optimal PTO damping coefficient in the range of $b_{pto}/(\rho_w g^{1/2} H_i^{5/2}) = 15$–20 As the wave period increases, the optimal PTO damping coefficient of the OB increases which is due to the in-phase motion of the OB with wave propagation. Fig. 8(b) indicated that the energy conversion efficiency of

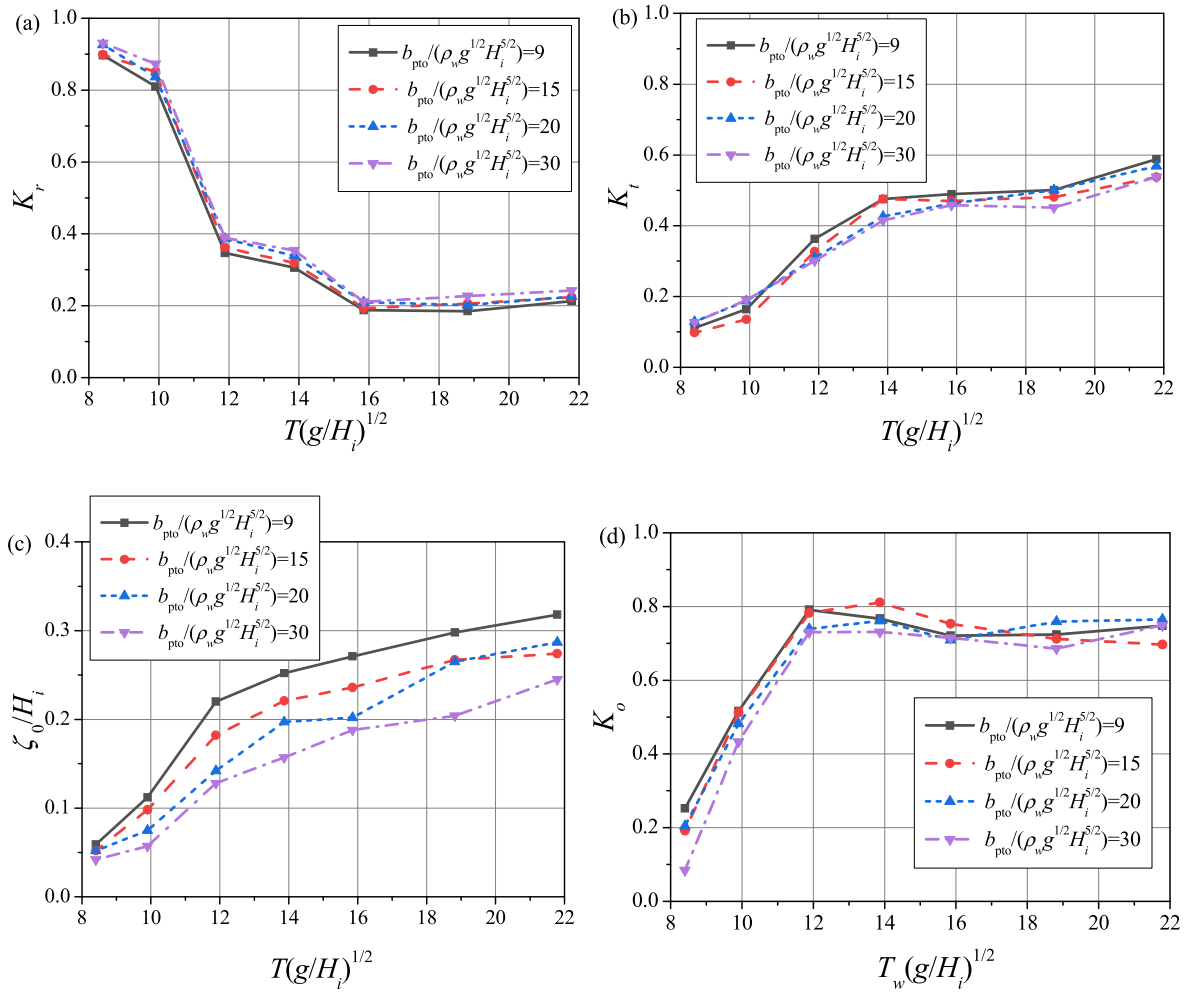

Fig. 14. Variations of (a) the reflection coefficient, (b) the transmission coefficient, (c) the heaving amplitude and (d) the wave coefficient with wave periods and hydraulic dampings.

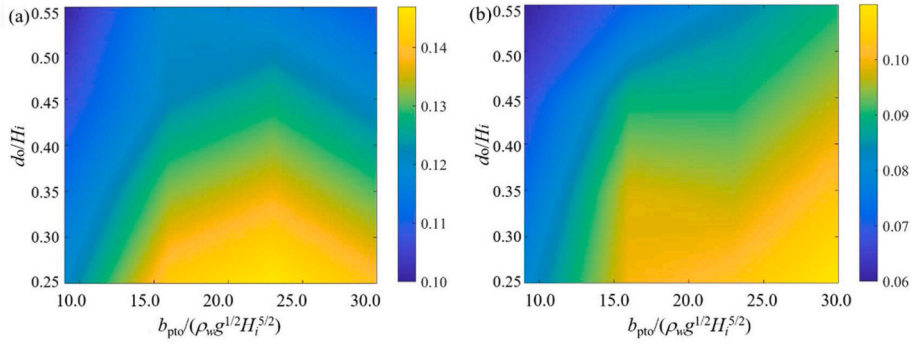

Fig. 15. Efficiency contour of (a) the OB and (b) the OWC within the hybrid-type WEC system as a function of pneumatic and hydraulic dampings.

the fixed OWC increases with increasing the opening diameter of the orifice, and is smaller in short-period waves and long-period waves, which is associated with the high reflection by the front pontoon in short-period waves and the high penetrability over the back pontoon in long-period waves. It is worth noting that although the maximum efficiency at $d_o/H_i = 0.45$ is lower than that at $d_o/H_i = 0.55$, it follows an opposite trend for the effective frequency bandwidth of $R > 0.1$.

4.2. Hydrodynamic performance of dual PTO systems

4.2.1. Effects of the pneumatic damping

In this sub-section, the complementary effect of the hydraulic-pneumatic hybrid PTO system is examined. Firstly, different pneumatic damping coefficients i.e. $d_o/H_i = 0.25$, 0.35, 0.45 and 0.55 are selected with a given hydraulic PTO damping $b_{pto}/(\rho_w g^{1/2} H_i^{5/2}) = 15$.

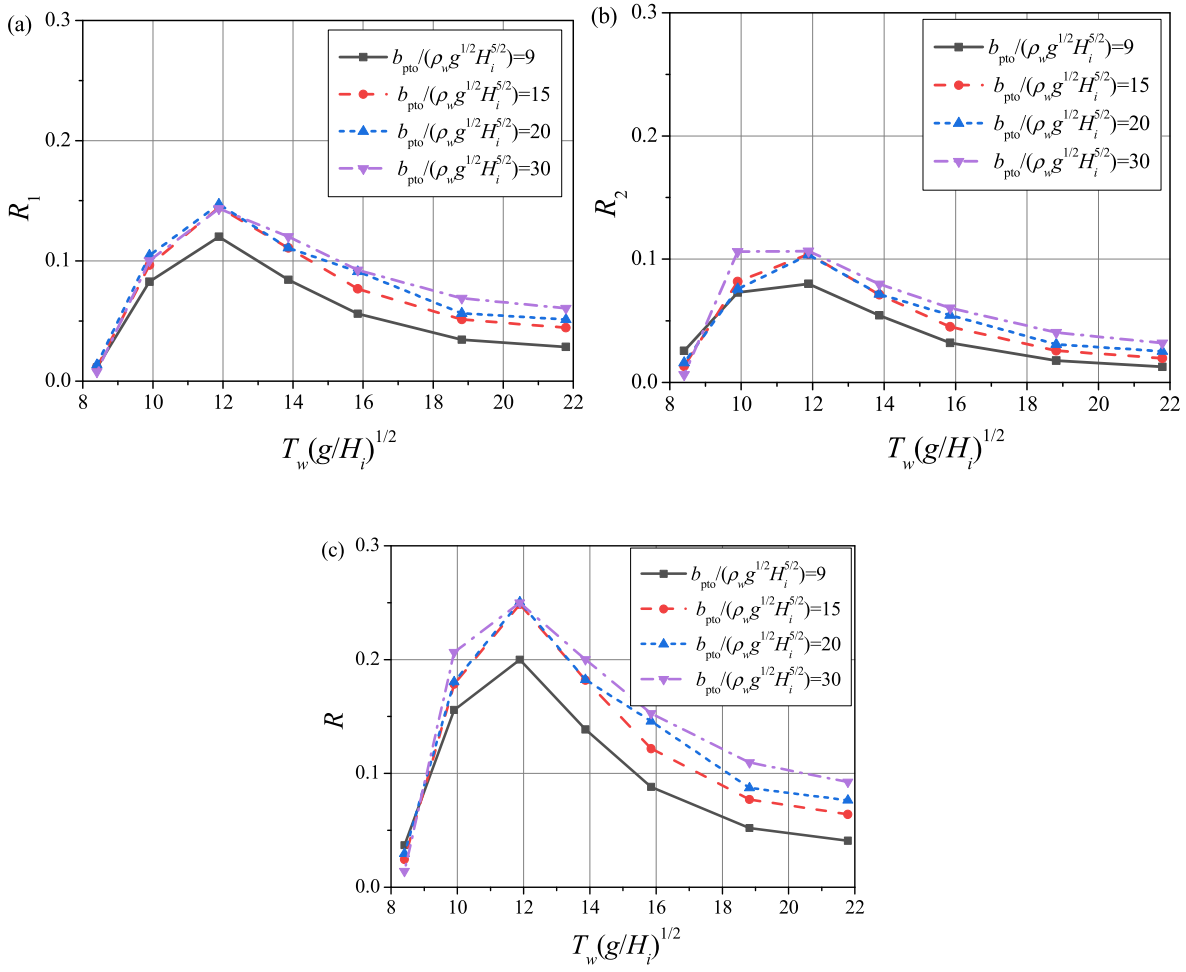

Fig. 16. Variations of the efficiency of (a) the OB, (b) the OWC and (c) the overall system with wave periods and hydraulic dampings.

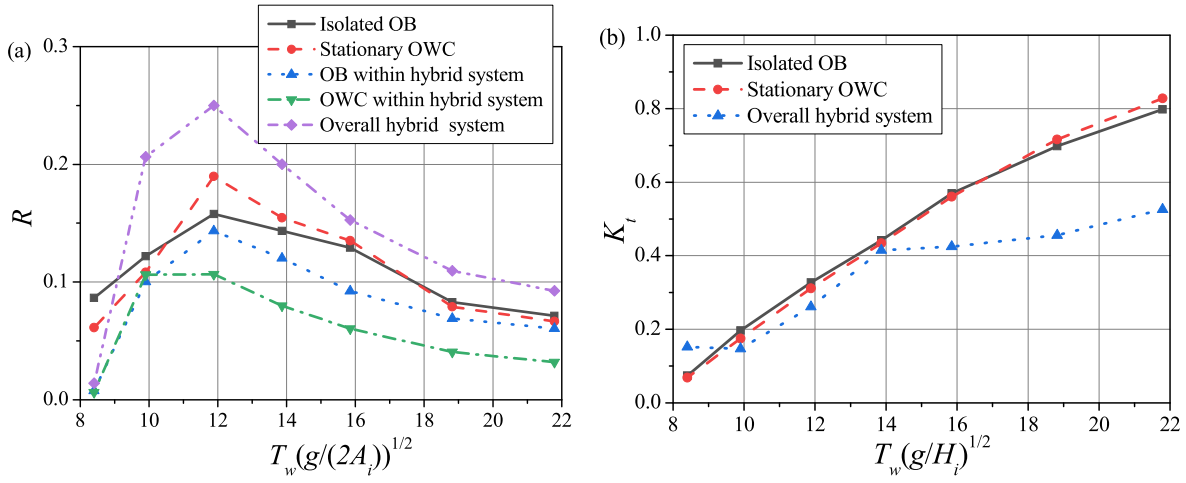

Fig. 17. Comparison of (a) the efficiency and (b) the transmission coefficient for different designs.

Other geometrical parameters are kept the same as those stated in Section 4.1. Fig. 9 displays the efficiency contour of the OB and OWC devices within the hybrid WEC system. It can be found that the wave energy harvested by each individual sub-device of the OB-OWC hybrid system is smaller than that harvested by the isolated OB and the OWC device, as shown in Fig. 8. It is reasonable that the motion of the pontoons is negatively related with the pneumatic pressure in the chamber between pontoons. Additionally, the maximum efficiency occurs d_o/H_i = 0.25 for the OB and OWC devices in the hybrid WEC system. Fig. 9(a) indicated that the resonant period $T_w(g/H_i)^{1/2}$ = 11.88 of the dual-pontoon OB is not sensitive to the variation of the pneumatic PTO damping. However, compared with the isolated OWC in Fig. 8(b), the optimal opening diameter of the orifice in the hybrid WEC system shifts to the smaller value, as shown in Fig. 9(b). As the opening diameter of the orifice increases, both the maximum efficiency and the effective frequency bandwidth decreases. Furthermore, the efficiency curves of

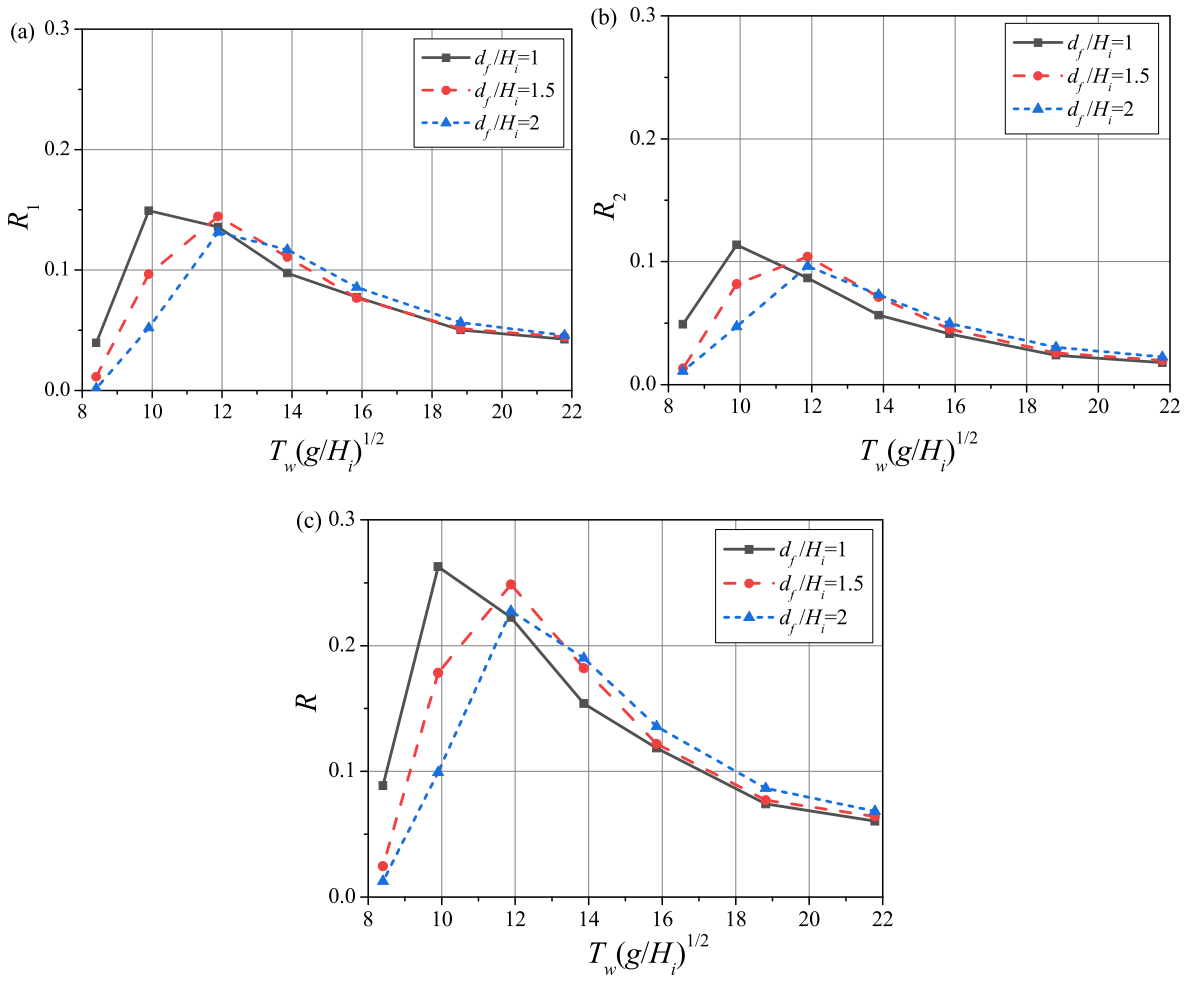

Fig. 18. Dependence of the efficiency of (a) the OB, (b) the OWC and (c) the overall system on pontoon drafts.

the OB, the OWC and the overall system with different wave periods and opening diameters are given in Fig. 10(a)–(c). From Fig. 10(a), it can be observed that the effect of the pneumatic damping on the wave energy conversion efficiency of the OB is mainly concentrated in the short-period wave region. In Fig. 10(b), the reduction in the energy conversion efficiency of the OWC device with increasing opening diameter is caused by the fact that the heave motion of the pontoons can strengthen the water motion in the chamber and enhance the wave transmission into the chamber, and thus the wave energy extraction is matched with a larger pneumatic damping for a fixed cross-section area of the water surface in the chamber. The pneumatic damping values are inversely proportional to the opening diameter of the orifice [11].

The variations in the transmission coefficient, the reflection coefficient, the heave motion and the wave coefficient in the chamber with nondimensional wave periods are shown in Fig. 11(a)–(d), respectively. From Fig. 11(a), it can be found that the reflection coefficient is almost unchanged by the opening diameter in the long-period wave region but increases with the opening diameter in the short-period wave region. This can be attributed to the reduction of the heave motion of the pontoons and waves are easily reflected by the facing-wave side. Fig. 11 (b) shows that the variation trend of the transmission coefficient with the opening diameter is different for short-, moderate- and long-wave regions. In the short-wave region, the transmission coefficient decreases slightly with the opening diameter, whereas it follows an opposite trend near the resonant period. In summary, the wave attenuation capacity of the hybrid system is insensitive to the variation of the pneumatic damping of the OWC.

It can be observed from Fig. 11(c) that for most of the wave periods tested in this paper, the heave response of the dual-pontoon floating body increases with increasing the pneumatic damping. This behaviour can be explained by the reason that the oscillating water response decreases with increasing the pneumatic damping, and the viscous drag force on the internal surface of the chamber is reduced which leads to a larger heaving travel of the pontoons. Therefore, for a given hydraulic PTO damping coefficient, the wave extraction of the OB in the hybrid system is enhanced by pneumatic damping, which is consistent with Fig. 9(a). In Fig. 11(d), the wave elevation in the chamber increases with increasing the opening diameter due to the reduction of the air pressure on the water plane inside the chamber.

In brief, although the wave energy extractions of both the OB and OWC in the hybrid WEC system are enhanced with a decreasing orifice diameter, the causations are different. For the OWC, the increase in efficiency is due to the internal water motion in the chamber leading to a larger optimal pneumatic damping, while for the OB, it is because of the reduction in the viscous drag force.

4.2.2. *Effects of the hydraulic damping*

Next, the orifice diameter was given as $d_o/H_i = 0.55$, and different PTO damping coefficients i.e. $b_{pto}/(\rho_w g^{1/2} H_i^{5/2}) = 9$, 15, 20 and 30 were selected for the OB. Fig. 12 shows the efficiency contour of the OB and OWC devices within the hybrid WEC system. By comparing Fig. 12 with Fig. 8, it is clear that the wave energy extractions of the OB and OWC within the hybrid WEC system are lower than those of the isolated respective devices across all hydraulic PTO damping coefficients. The optimal PTO damping coefficient for the OB is basically unaffected by the additional OWC, as shown in Fig. 12(a). As the b_{pto} increases, both

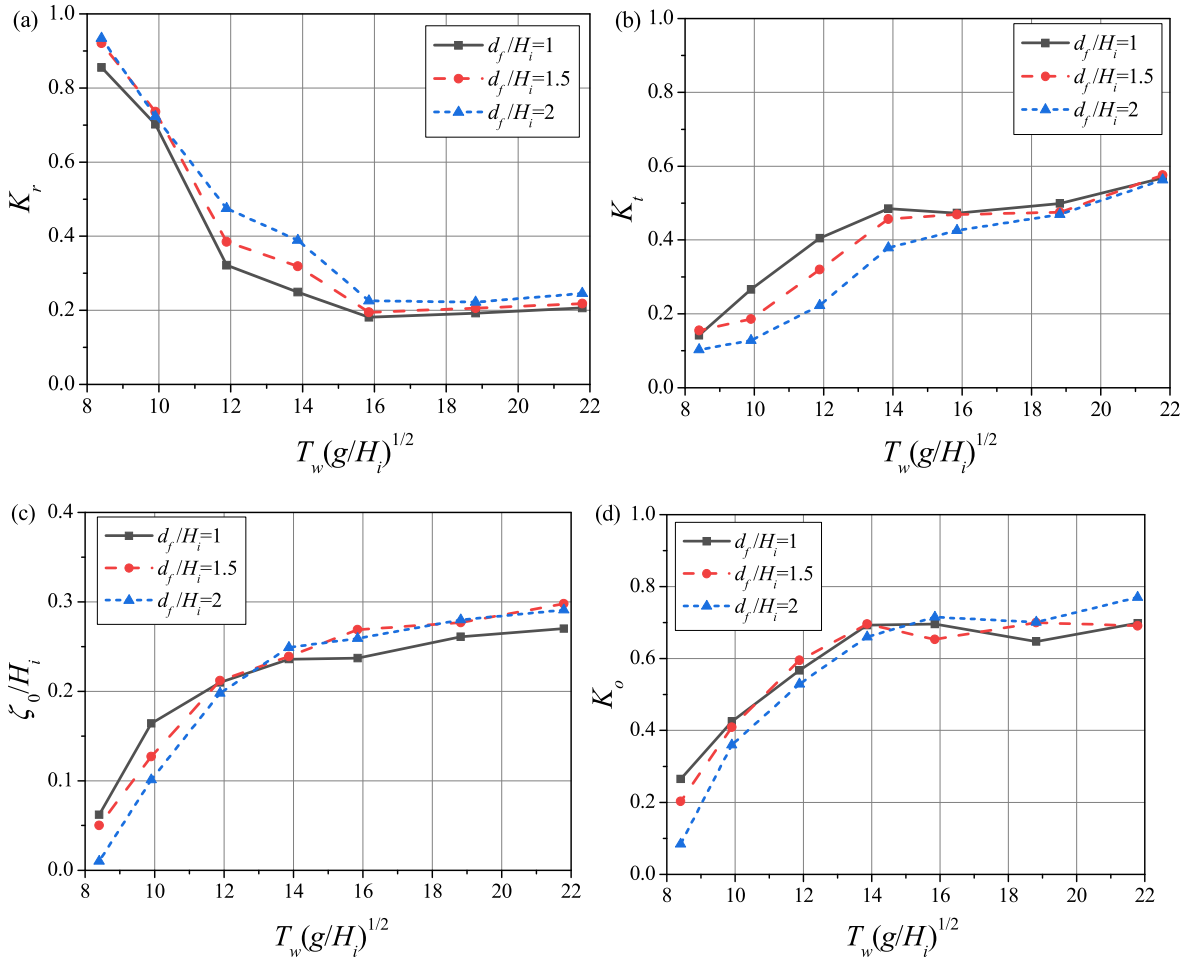

Fig. 19. Dependence of (a) the reflection coefficient, (b) the transmission coefficient, (c) the heaving amplitude and (d) the wave coefficient on pontoon drafts.

the energy conversion efficiency and the effective frequency bandwidth increase for the OWC, as shown in Fig. 12(b). Such a performance can be explained by the heave motion of the pontoons can reduce the variation of the air pressure induced by the water motion in the chamber.

Fig. 13 shows the efficiency curves of the OB, the OWC and the overall system under different wave periods and hydraulic PTO dampings. In Fig. 13(a), the OB wave energy conversion efficiency is almost identical in short-wave regions for different PTO dampings. This illustrates that the increase in the PTO damping cancels the reduction of the motion of the pontoons, leading to unchanged wave energy extraction. The energy conversion efficiency of the OB with PTO damping increases monotonically in the long-wave region. At the resonant period $T_w(g/H_i)^{1/2} = 11.88$, the energy conversion efficiency increases with increasing PTO damping and then slightly decreases after $b_{pto}/(\rho_w g^{1/2} H_i^{5/2}) = 20$. Similar trends are also found in Fig. 13(b), which further suggests that larger motion of the chamber with smaller PTO damping partly conflicts with wave energy extraction of the OWC. However, the maximum efficiency of the overall hybrid system occurs at about $b_{pto}/(\rho_w g^{1/2} H_i^{5/2}) = 20$, and is almost unchanged as b_{pto} further increases. This suggests that there exist complementary effects between the hydraulic and the pneumatic PTO dampings to adjust the optimal wave energy extraction of the hybrid WEC system.

Moreover, since the superposition of the scattering waves by the pontoons and the pressure-forced water plane in the chamber becomes more prominent at the facing-wave location near the hybrid system, the reflection coefficient of the hybrid WEC system increases with increasing b_{pto}, as shown in Fig. 14(a), and an adverse behaviour is seen for the transmission coefficient in Fig. 14(b). As can be intuitively anticipated, the heave motion of the dual-pontoon floating body decreases with increasing the PTO damping b_{pto}, as shown in Fig. 14(c). Referring to Fig. 14(d), the wave elevation in the chamber decreases with increasing the PTO damping b_{pto} for the short-wave region, which can be explained by the stronger reflection indicated in Fig. 13(a). For long-wave regions, the variation of the wave elevation with b_{pto} is irregular due to various factors i.e. high penetrability of long waves, heave motion of pontoons and air pressure fluctuation in the chamber.

4.2.3. *Synchronous control of the pneumatic and hydraulic dampings*

So far, the effects of two PTO systems have been individually studied as a function of the opening diameter or the PTO damping coefficient. Then, what will happen if the damping coefficients corresponding to two PTO systems change simultaneously? To explain this question, a series of physical tests have been performed by adjusting d_o/H_i from 0.25 to 0.55 and $b_{pto}/(\rho_w g^{1/2} H_i^{5/2})$ from 9 to 30 while keeping the same wave period at the resonant period $T_w = 1.2$ s. The efficiency contour of wave energy extraction is displayed in Fig. 15. It is clear that smaller opening diameters i.e. $d_o/H_i = 0.25$ lead to higher wave energy extraction. The optimal hydraulic PTO damping are $b_{pto}/(\rho_w g^{1/2} H_i^{5/2}) = 20$ and 30 for OB and OWC, respectively. Furthermore, the opening diameter is fixed as the minimum value $d_o/H_i = 0.25$, and the effects of different $b_{pto}/(\rho_w g^{1/2} H_i^{5/2}) = 9$, 15, 20 and 30 on the energy conversion efficiency are given in Fig. 16 as a function of wave periods. It is remarkable that the varying trend of the wave energy extraction with different b_{pto} is similar within the entire tested wave period range. The maximum value of the overall efficiency occurs at $b_{pto}/(\rho_w g^{1/2} H_i^{5/2}) = 15$ and presents the narrow spread with further increasing b_{pto}, as plotted in Fig. 16(c).

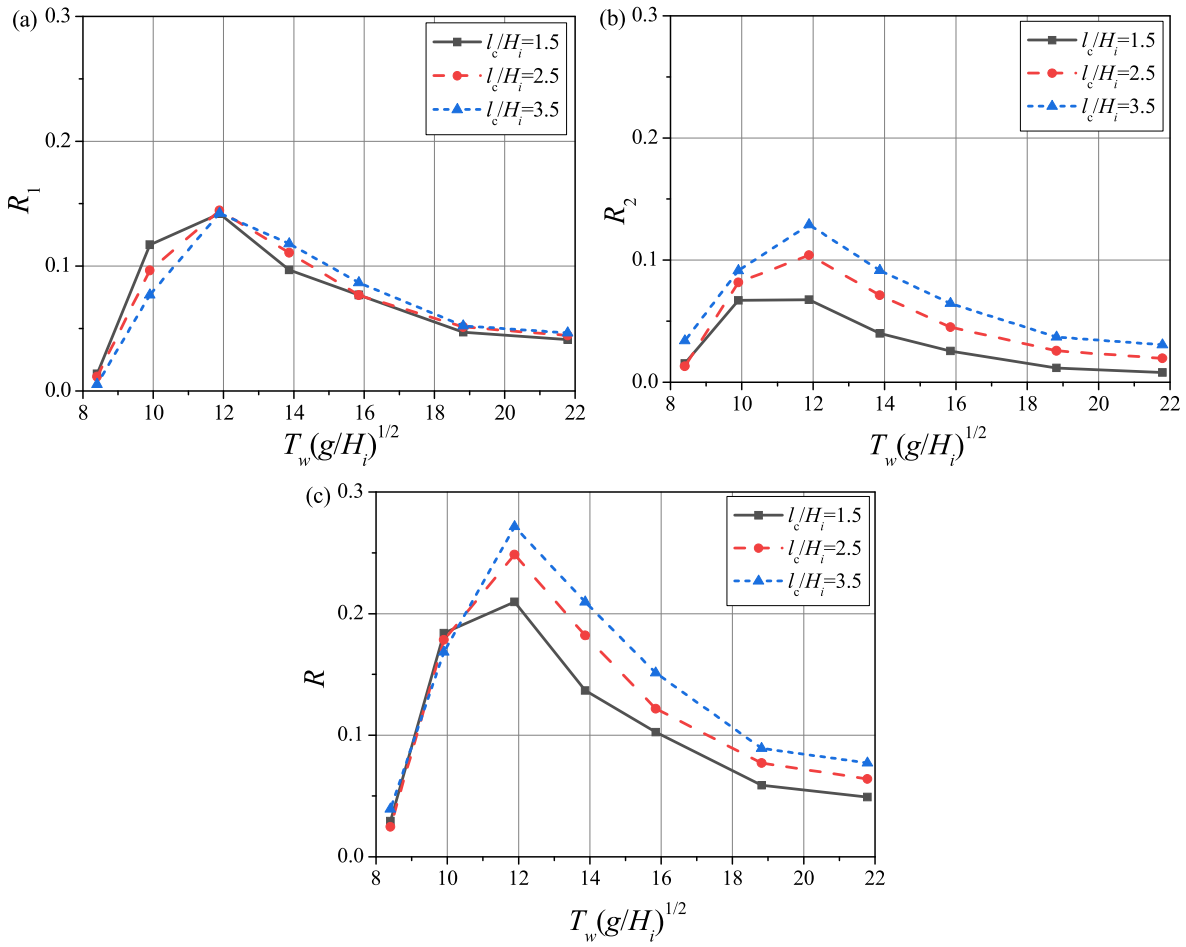

Fig. 20. Dependence of the efficiency of (a) the OB, (b) the OWC and (c) the overall system on chamber widths.

In general, the optimal opening diameter and the PTO damping coefficient are $d_o/H_i = 0.25$ and $b_{pto}/(\rho_w g^{1/2} H_i^{5/2}) = 15$ for the hybrid WEC system. The efficiency and transmission coefficient of the overall hybrid system, the sub-devices, and respective isolated devices are compared in Fig. 17(a) and (b) when the optimal PTO dampings are considered in the tested models. From Fig. 17(a), it can be found that the efficiency of the sub-devices within the hybrid WEC system is lower than that of the isolated devices, while the maximum efficiency of the overall hybrid system is about 25% higher than that of the isolated devices at the resonant periods. The frequency bandwidth of harvesting energy with $R > 0.1$ is significantly extended. The efficiency curves of the OB and OWC within the hybrid system tend to have the same variation with wave period due to the overlap of their resonant periods, and the high wave energy extraction of the OB in long waves recoups the energy loss of the OWC induced by the motion of the chamber. Fig. 17(b) shows that the transmission coefficient is effectively diminished by the hybrid WEC system due to more wave energy exchange from the incident waves to WECs, especially for long-period waves. This will substantially modify the hydrodynamic defect of the floating breakwater in long waves. Another noteworthy phenomenon is that both the wave energy extraction and the wave attenuation at extreme short waves i.e. $T_w(g/H_i)^{1/2} = 8.4$ are reduced by the hybrid system compared with the stationary OWC.

4.3. Effects of the pontoon draft

It is well known that the pontoon draft has a significant influence on the resonant periods and the wave energy absorption of the WEC-breakwater system. Three pontoon drafts i.e. $d_f/H_i = 1$, 1.5 and 2 are considered, and the optimal PTO parameters are applied with other same parameters stated in Section 4.2. Fig. 18 presents the energy conversion efficiency of the OB, the OWC and the overall system. The resonant periods of the OB and the water in the chamber shift to larger values with increasing the pontoon draft. The maximum efficiencies at the resonant periods decrease with the pontoon draft. For example, the efficiencies with $d_f/H_i = 1$, 1.5 and 2 are 0.15, 0.14 and 0.12 for the OB, and those are 0.11, 0.10 and 0.09 for the OWC. Such reduction is due to wave energy decaying along the water depth [30]. It is interesting that the effects of the pontoon draft are more remarkable in short waves than those in long waves. Short waves with weak transmission are more sensitive to the pontoon draft and more components are reflected by deeper pontoons. Conversely, long waves with strong transmission are insensitive to the variation of the pontoon draft.

Fig. 19 displays the reflection coefficient, the transmission coefficient, the heave response and the wave coefficient in the chamber for different pontoon drafts. It can be observed from Fig. 19(a) that the reflection coefficient with $d_f/H_i = 0.1$ is the smallest among the three pontoon drafts due to the reduction of the effective seaward area, especially near the resonant period. Changing the pontoon draft did not modify the variation of K_r against T_w. The transmission coefficient in Fig. 19(b) reduces with increasing pontoon draft for short-period waves, but is not sensitive for long-period waves. This is mainly attributed to the contribution of the reflection coefficient. The variation of the heave motion of the chamber is in accordance with that of the wave coefficient in the chamber. It is not a surprise that the wave load on the bottom of the pontoons decreases with increasing the pontoon draft, and the heave motion reduces accordingly. On the other hand, the water mass in the chamber increase with increasing the pontoon draft, which means that

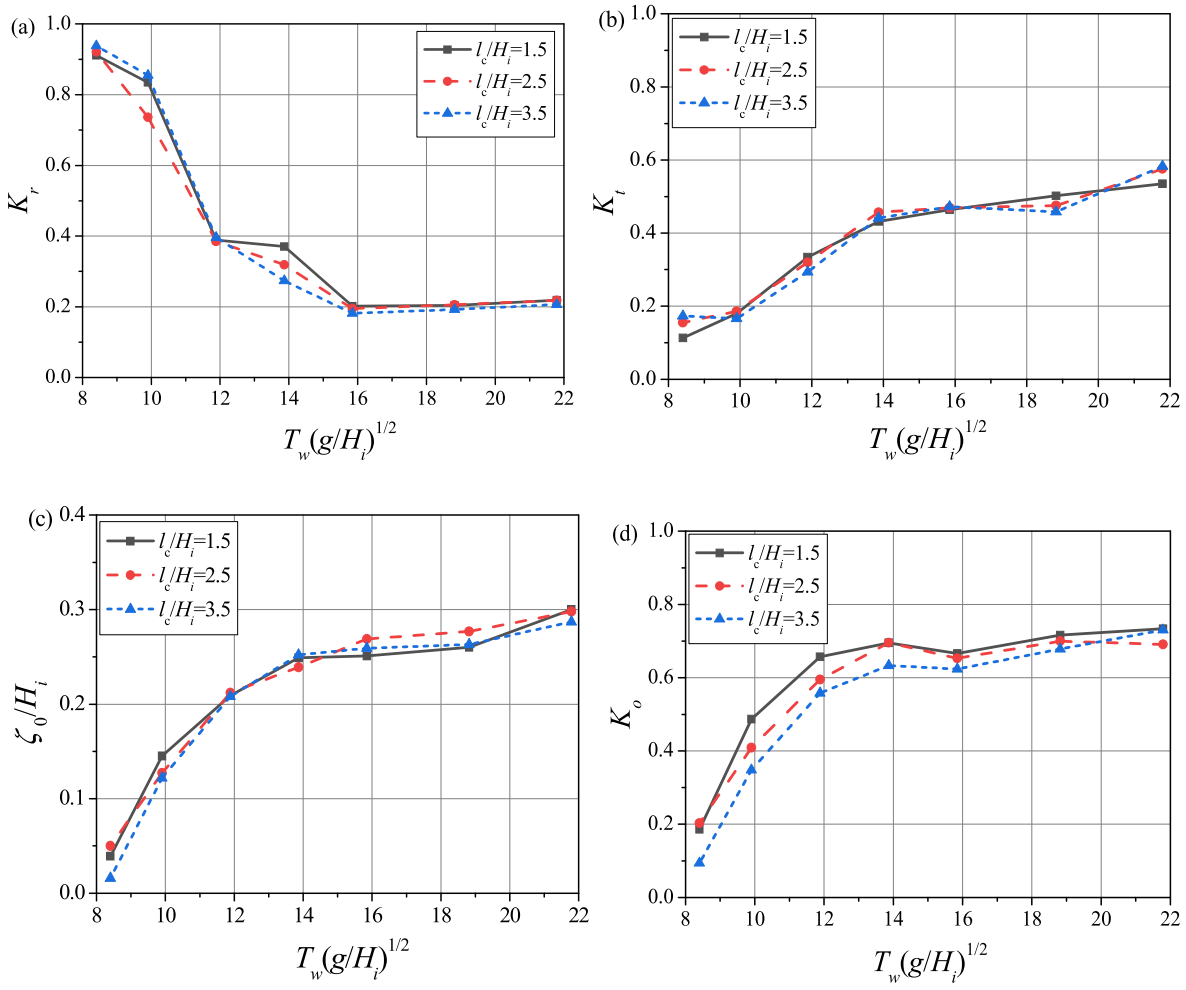

Fig. 21. Dependence of (a) the reflection coefficient, (b) the transmission coefficient, (c) the heaving amplitude and (d) the wave coefficient on chamber widths.

the same water motion in the chamber should be excited by a larger wave force.

4.4. Effects of the chamber width

The sub-section examines the effects of different chamber widths i.e. $l_c/H_i = 1.5$, 2.5 and 3.5 while each pontoon width is fixed as $b/H_i = 1.5$. The pontoon draft is also kept unchanged, i.e. $d_f/H_i = 1.5$ and other parameters have been given in Section. 4.3. Fig. 20 displays the harvesting efficiency of the OB, OWC and overall system for different chamber widths. It can be concluded from Fig. 20(a) that the resonant heave period i.e. $T_w(g/H_i)^{1/2} = 12$ of the OB is the same among there chamber width. In the wave region of $T_w(g/H_i)^{1/2} < 12$, the harvesting efficiency of the OB decreases with increasing chamber width, but it follows a contrary trend when $T_w(g/H_i)^{1/2} > 12$. In Fig. 20(b), the harvesting efficiency of the OWC is improved by a larger chamber width for the whole tested wave period range. The reason can be found from Eq. (5), which indicates that wave energy extraction of the OWC increases linearly with an increasing cross-section area of the chamber. By comparing Fig. 20(a) and (b), the effects of the distance between pontoons on the OWC is more significant than those on the OB, and thus a larger chamber width leads to a higher overall efficiency of the hybrid WEC system, as shown in Fig. 20(c).

Fig. 21(a)–(d) displays the reflection coefficient, the transmission coefficient, the heave motion and the wave coefficient in the chamber for different chamber widths. The effects of the chamber width are less dominant on the reflection coefficient, the transmission coefficient and the heave motion of the OB. This indicates that the attenuation capacity of the floating breakwater depends mainly on the structural surface interacting with waves. However, it should be noted that the wave elevation in the chamber diminishes with increasing chamber width. This is due to the fact that the opening ratio of the orifice decreases with chamber width, leading to a larger pneumatic damping. Hence, a larger air pressure is reflected to mitigate the water column motion in the chamber.

5. Conclusion

This paper presents an experimental investigation on the hydrodynamic performance of a pile-supported dual-pontoon floating breakwater which holds the function of wave energy converters (WECs) concurrently. The base structure is regarded as an OB device with a hydraulic PTO system installed at its top, and the chamber between dual pontoons is constructed as an OWC device. The complementary effects between the hydraulic and pneumatic PTO systems were specially examined by adjusting individually and synchronously PTO damping coefficients. Besides, the hydrodynamic differences among different pontoon drafts and chamber widths were also emphasised. The following findings can be obtained from this study:

(1) Due to the fact that the heave motion of the chamber and the internal air pressure cancel mutually, the respective conversion efficiency of sub-devices within the hybrid system is reduced, but

the overall hybrid system possesses higher energy extraction compared with the isolated OB and the stationary OWC.

(2) Comparisons of different combinations between the two PTO systems illustrated that the motion of the chamber leads to a larger optimal PTO damping for the OWC, while the optimal PTO damping for the OB is almost unaffected by the OWC. The effects of the pneumatic PTO damping on the OB and OWC focus mainly on short-period and long-period waves, respectively. However, the effects of the hydraulic PTO damping are embodied in long-period waves for both devices.

(3) When the pneumatic and hydraulic PTO dampings are adjusted simultaneously, the optimal pneumatic PTO damping is identical between the two sub-devices, while the optimal hydraulic PTO damping for the OWC is larger than that for the OB. Accordingly, under the premise of guaranteeing the wave energy extraction of the OB, a larger hydraulic PTO damping is favourable to mitigate the conflict between the chamber motion and the internal air pressure.

(4) More energy transferring from water waves to the hydraulic-pneumatic hybrid system significantly reduces the transmission coefficient in long-period waves, which is constructive for enhancing the wave attenuation capacity of the floating breakwater.

(5) The effects of the pontoon draft on the maximum energy extraction and the wave attenuation are adverse. For example, a deeper pontoon is beneficial for wave attenuation but becomes disadvantageous for maximum energy conversion efficiency.

(6) Increasing chamber width cannot enhance the wave attenuation capacity but can improve the overall energy conversion efficiency for the entire tested wave period range, which is mainly contributed by the OWC device.

It should be emphasised that integrating two independent PTO technologies on a floating foundation would add the design complexities of the hybrid WEC system, which is associated with the higher Levelised Cost of Electricity (LCOE). In addition to the performance tests under regular waves, it could be physically more realistic to study problems as being under irregular waves. In future work, the effects of irregular waves on both economic competitiveness and the coupled hydrodynamic interaction will be evaluated for the hybrid WEC system. It should be noted that the findings of this paper are based on two-dimensional experiments, and some three-dimensional effects of wave field, i.e. three-dimensional scattering waves and oblique waves are not covered by the physical experiments, which will be studied in the future.

CRediT authorship contribution statement

Yong Cheng: Conceptualisation, Formal analysis, Writing-original draft, Supervision, Funding acquisition; **Fukai Song:** Data curation, Formal analysis, Writing-original draft; **Lei Fu:** Software, Writing-original draft, Investigation; **Saishuai Dai:** Formal analysis, Data curation, Writing-review & editing, Supervision; **Zhiming Yuan:** Writing-review & editing; **Atilla Incecik:** Supervision.

Declaration of competing interest

The authors declare that they have no known competing financial interests or personal relationships that could have appeared to influence the work reported in this paper.

Data availability

Data will be made available on request.

Acknowledgement

The authors are grateful to the National Natural Science Foundation of China (Grant No. 52111530137), a the Newton Advanced Fellowships (Grant No. NAF\R1\180304) by the Royal Society for supporting this work.

References

[1] European Commission. 2014, 2030 Climate & Energy Framework [Online]. Available: https://eur-lex.europa.eu/eli/dir/2012/27/202 1-01-01. [Accessed 1 April 2022].
[2] Gallutia G, Fard MT, Soto MG. Recent advances in wave energy conversion systems: from wave theory to devices and control strategies. Ocean Eng 2022;252:111105.
[3] Korde UA, Ringwood J. Hydrodynamic control of wave energy devices. Cambridge University Press; 2016. p. 151–81.
[4] Guo BY, Ringwood JV. Geometric optimisation of wave energy conversion devices: a survey. Appl Energy 2021;297:117100.
[5] Ocean Energy Europe (OEE). Key trends and statistics 2021. 2022. _Stats_2021_web.
[6] Falcão AFO, Henriques JCC. Oscillating-water-column wave energy converters and air turbines: a review. Renew Energy 2016;85:1391–424.
[7] He F, Huang ZH. Hydrodynamic performance of pile-supported OWC-type structures as breakwaters: an experimental study. Ocean Eng 2014;88:618–26.
[8] Konispoliatis DN, Mavrakos SA. Hydrodynamic analysis of an array of interacting free-floating oscillating water column (OWC's) devices. Ocean Eng 2016;111:179–97.
[9] Ning DZ, Shi J, Zou QP, Teng B. Investigation of hydrodynamic performance of an OWC (oscillating water column) wave energy device using a fully nonlinear HOBEM (higher-order boundary element method). Energy 2015;83:177–88.
[10] Ning DZ, Wang RQ, Zou QP, Teng B. An experimental investigation of hydrodynamics of a fixed OWC Wave Energy Converter. Appl Energy 2016;168:636–48.
[11] Ning DZ, Zhou Y, Zhang CW. Hydrodynamic modeling of a novel dual-chamber OWC wave energy converter. Appl Energy Res 2018;78:180–91.
[12] Molina A, Jimenez-Portaz M, Clavero M, Monino A. The effect of turbine characteristics on the thermodynamics and compression process of a simple OWC device. Renew Energy 2022;190:836–47.
[13] Portillo JCC, Reis PF, Henriques JCC, Gato LMC, Fallcao AFO. Backward bent-duct buoy or frontward bent-duct buoy? Review, assessment and optimisation. Renew Sustain Energy Rev 2019;112:353–68.
[14] Windt C, Davidson J, Ringwood JV. Numerical analysis of the hydrodynamic scaling effects for the Wavestar wave energy converter. J Fluid Struct 2021;105:103328.
[15] Kramer M, Marquis L, Frigaard P. Performance evaluation of the Wavestar prototype. Proceedings of the 9th European wave and tidal conference (EWTEC), Southamption, UK. 2011.
[16] Zhang WC, Liu HX, Zhang L, Zhang XW. Hydrodynamic analysis and shape optimisation for vertical axisymmetric wave energy converters. China Ocean Eng 2016;30:954–96.
[17] Renzi E, Doherty K, Henry A, Dias F. How does Oyster work? The simple interpretation of Oyster mathematics. Eur J Mech B Fluid 2014;47:124–31.
[18] Goggins J, Finnegan W. Shape optimisation of floating wave energy converters for a specified wave energy spectrum. Renew Energy 2014;71:208–20.
[19] Wang YH, Wang DX, Dong S. A theoretical model for an integrated wave energy extraction system consisting of a heaving buoy and a perforated wall. Renew Energy 2022;189:1086–101.
[20] Robertson B, Bailey H, Leary M, Buckham B. A methodology for architecture agnostic and time flexible representations of wave energy converter performance. Appl Energy 2021;287:116588.
[21] Shahbaz M, Balsalobre-Lorente D. Econometrics of green energy handbook. Springer; 2020.
[22] Correia da Fonseca FX, Gomes RPF, Henriques JCC, Gato LMC, Falcao AFO. Model testing of an oscillating water column spar-buoy wave energy converter isolated and in array: motions and mooring forces. Energy 2016;112:1207–18.
[23] Cui L, Zheng SM, Zhang YL, Miles J, Iglesias G. Wave power extraction from a hybrid oscillating water column-oscillating buoy wave energy converter. Renew Sustain Energy Rev 2021;135:110234.
[24] Dong S, Wang YH. Theoretical investigation on integrating a torus oscillating body with a concentric perforated cylindrical system. Ocean Eng 2021;24:110122.
[25] Cheng Y, Du WM, Dai SS, Ji CY, Collu M, Cocard M, et al. Hydrodynamic characteristics of a hybrid oscillating water column-oscillating buoy wave energy converter integrated into a π-type floating breakwater. Renew Sustain Energy Rev 2022;161:112299.
[26] Cheng Y, Fu L, Dai SS, Collu M, Cui L, Yuan ZM, et al. Experimental and numerical analysis of a hybrid WEC-breakwater system combining an oscillating water column and an oscillating buoy. Renew Sustain Energy Rev 2022;169:112909.
[27] Nguyen HP, Wang CM, Luong VH. Two-mode WEC-type attachment for wave energy extraction and reduction of hydroelastic response of pontoon-type VLFS. Ocean Eng 2020;197:106875.

[28] Mustapa MA, Yaakob OB, Ahmed YM, Rheem CK, Koh KK, Adnan FA. Wave energy device and breakwater integration: a review. Renew Sustain Energy Rev 2017;77:43–58.
[29] Zhao XL, Ning DZ, Zou QP, Qiao DS, Cai SQ. Hybrid floating breakwater-WEC system: a review. Ocean Eng 2019;186:106126.
[30] He F, Zhang HS, Zhao JJ, Zheng SM, Iglesias G. Hydrodynamic performance of a pile-supported OWC breakwater: an analytical study. Appl Ocean Res 2019;88:326–40.
[31] Guo BM, Ning DZ, Wang RQ, Ding BY. Hydrodynamics of an oscillating water column WEC - breakwater integrated system with a pitching front-wall. Renew Energy 2021;176:67–80.
[32] Howe D, Nader J, Macfarlane G. Experimental investigation of multiple oscillating water column wave energy converters integrated in a floating breakwater: energy extraction performance. Appl Ocean Res 2020;97:102086.
[33] Zhang HM, Zhou BZ, Vogel C, Wilden R, Zang J, Zhang L. Hydrodynamic performance of a floating breakwater as an oscillating-buoy type wave energy converter. Appl Energy 2019;257:113996.
[34] Zhao XL, Zhang LD, Li MW, Johanning L. Experimental investigation on the hydrodynamic performance of a multi-chamber OWC-breakwater. Renew Sustain Energy Rev 2021;150:111512.
[35] Cheng Y, Fu L, Dai SS, Collu M, Yuan ZM, Incecik A. Experimental and numerical investigation of WEC-type floating breakwaters: a single-pontoon oscillating buoy and a dual-pontoon oscillating water column. Coast Eng 2022;177:104188.
[36] Goda Y, Suzuki Y. Estimation of incident and reflected waves in random wave experiments. Proceedings of the 15th international conference on coastal engineering ASCE. 1976. p. 828–45.
[37] Fossa M, Guglielmini G. Pressure drop and void fraction profiles during horizontal flow through thin and thick orifices. Exp Therm Fluid Sci 2002;26:513–23.
[38] Mei CC, Stiassnie M, Yue DKP. Theory and applications of ocean surface waves. World Scientific Publishing Co Pte Ltd; 2005.
[39] Maia AAG, Cavalca DF, Tomita JT, Costa FP, Bringhenti C. Evaluation of an effective and robust implicit time-integration numerical scheme for Navier-Stokes equations in a CFD solver for compressible flows. Appl Math Comput 2022;413:126612.